Journal of Materials Chemistry A

PAPER

View Article Online
View Journal | View Issue

Cite this: J. Mater. Chem. A, 2014, 2, 5077

Post-heating effects on the physical and electrochemical capacitive properties of reduced graphene oxide paper†

Sikandar H. Tamboli, Beom Seok Kim, Geehong Choi, Hwanseong Lee, Donghwi Lee, U. M. Patil, Juhwan Lim, S. B. Kulkarni, Seong Chan Jun and Hyung Hee Cho*

Received 14th January 2014
Accepted 24th January 2014

DOI: 10.1039/c4ta00209a

www.rsc.org/MaterialsA

We report combined electrochemical double-layer capacitance (EDLC) and pseudocapacitance in reduced graphene oxide (rGO) thick film like paper due to annealing temperature variations. The influence of annealing temperature (from room temperature (RT) to 1000 °C) on the structural, morphological, electrical, and electrochemical properties of rGO paper was evaluated. Upon increasing the annealing temperature, shifting of the dominant (002) X-ray diffraction (XRD) peak to a higher degree, volume expansion, and red-shifting of the G band in Raman spectra were observed. High-resolution transmission electron microscopy (HRTEM) images showed a reduction in the interlayer distance in rGO sheets from 0.369 to 0.349 nm as the annealing temperature increased from RT to 1000 °C; these results were congruent with the XRD results. According to X-ray photoelectron spectroscopy (XPS), the presence of hydroxyl, carboxyl, and other oxygen-containing groups decreased in samples annealed at higher temperatures. The attached functional groups, the electrical conductivity, and the supercapacitance of rGO papers were found to be mutually interrelated and could be tuned by varying the annealing temperature. The rGO paper annealed at 200 °C in a 1 M H_2SO_4 electrolyte at a scan rate of 50 mV s^{-1} exhibited a maximum specific capacitance of 198 F g^{-1}.

1. Introduction

The rising price of fossil fuels, together with their rapid depletion and pollution caused by their combustion,[1] has intensified the search for clean renewable energy sources and energy-storage devices.[2] Among energy-storage devices, supercapacitors, also known as electrochemical capacitors (EC) or ultracapacitors, are quite attractive, because they can provide higher power density than batteries or fuel cells and much higher energy density than conventional capacitors.[3,4] Supercapacitors are generally classified as having either electrical double-layer capacitance (EDLC) or pseudocapacitance. EDLCs store energy through accumulated charge at the interface between an electrode and an electrolyte. The EDLC energy-storage mechanism allows for long-term stability and fast charge–discharge.[4]

Carbon materials (activated carbon, carbon aerogels, mesoporous carbon, carbon spheres, carbon nanotubes, graphene, *etc.*) have been used in commercial EDLC supercapacitors because of their high specific surface area, thermal stability, high conductivity, and excellent corrosion resistance to electrolytes.[5–12] Graphene is an emerging carbon nanomaterial consisting of monolayered sp^2 hybrid carbon atoms; recently, graphene has been a hotly discussed material for potential use in flexible supercapacitors, batteries, and sensor applications because of its superior properties compared to other carbon materials.[6,13] The scientific and technological significance of graphene-based electrodes is widely appreciated; the material is particularly renowned for enabling high power density in energy-storage devices, and it has been shown to be an ideal carbon-based electrode material for EDLCs. For example, graphene exhibits highly proficient double-layer capacitance, with a theoretical value up to 550 F g^{-1} for a fully utilized surface area of 2675 m^2 g^{-1}.[13] Diverse carbon-based materials have also been evaluated for use in EDLCs; however, their specific capacitance, energy density, and power density values have proven to be lower than anticipated.[5–8,13–15]

In energy-storage devices, freestanding, multilayered graphene paper has proven highly useful.[16–18] Multilayered graphene papers can be prepared by lamination of graphene sheets obtained *via* a hydrothermal process,[19] chemically reduced graphene oxide (GO) sheets pressed into a paper form *via* vacuum filtration,[20,21] chemical or laser scribed reduction of GO papers to form reduced graphene oxide (rGO) papers[14,22] are well known. Among these methods, chemical reduction of GO papers to form rGO is the simplest way, and rGO papers made

Department of Mechanical Engineering, Yonsei University, 50 Yonsei-ro, Seodaemun-gu, Seoul 120-749, Korea. E-mail: hhcho@yonsei.ac.kr; Fax: +82 2 312 2159; Tel: +82 2 2123 2828

† Electronic supplementary information (ESI) available. See DOI: 10.1039/c4ta00209a

via chemical reduction possess several favorable properties, including good conductivity, catalytic properties, and high mechanical strength.[22]

Numerous studies have reported the fabrication and development of multilayered rGO paper. One-spot reduction of GO using the reducing agent sodium–ammonia solution at low temperature was described by Feng *et al.*[23] Chen *et al.* reported the use of chemical reduction of individual GO sheets in an aqueous dispersion using hydrazine hydrate to form rGO sheets followed by flow-directed vacuum filtration.[21] Sun *et al.* reported the flame-induced reduction of GO paper for supercapacitor applications.[24] Electrical conductivity improvement upon gentle annealing of GO paper was studied by Valles *et al.*[25] In addition, composites of rGO powder and paper with various metal oxides and polymers have been extensively studied for supercapacitor electrode applications.[26–30]

The specific area, the presence of attached functional groups, and electrical conductivity of graphene or rGO play crucial roles in supercapacitor electrode performance. Furthermore, these factors are interlinked with annealing temperature. In this study, rGO paper was obtained by GO paper reduction using hydriodic acid (HI). The influence of annealing temperature (from RT to 1000 °C) on structural behavior, surface morphology, interlayer spacing, and specific capacitance of obtained paper was evaluated.

2. Experimental section

2.1 Materials and methods

rGO paper preparation involves the following steps: (i) preparation of GO and its paper and (ii) preparation of rGO paper *via* reduction of GO paper.

GO was prepared by chemical oxidation of graphite flecks powder according to a modified Hummers' method. Graphite flecks powder (1.5 g, 325 mesh, SP-1, Bay Carbon, USA), $K_2S_2O_8$ (2.5 g, 99.99% purity, Sigma-Aldrich, USA), and P_2O_5 (2.5 g, 99.99% purity, Sigma-Aldrich, USA) were mixed with concentrated H_2SO_4 (12 mL, extra pure grade, Duksan Pure Chemicals, Korea). The solution was heated to 80 °C with continuous stirring in an oil bath for 5 h. The mixture was then cooled to room temperature, diluted with deionized (DI) water (500 mL), and kept overnight. Then, the product was obtained by filtration using a 0.2 μm nylon film and drying at 60 °C. Pre-treated graphite powder was kept at 0 °C in concentrated H_2SO_4 (120 mL); soon after, $KMnO_4$ (15 g, Junsei Chemical Co. Ltd, Japan) was added gradually while stirring. The temperature of the mixture was maintained below 10 °C using an ice bath during $KMnO_4$ addition. The mixture was then stirred at 35 °C for 4 h and then diluted with 700 mL of DI water. H_2O_2 (30 mL, 30 wt% in H_2O, Sigma-Aldrich, USA) was added drop by drop. The resultant bright-yellow suspension was obtained. It was washed with 1 : 10 HCl aqueous solution (35–37% extra pure, Samchun Pure Chemicals, Korea) to remove metal ions followed by 1 L of deionized water to remove the acid using a centrifuge machine (Supra 22K Hanil BioMed Inc. Korea). Finally, the material was purified using dialysis for 1 week to remove remaining metal species. The resulting gel like solution was used for GO paper preparation. It was dried in a Petri dish at 60 °C for 48 h, and the prepared thin GO paper was peeled off carefully.

The GO paper was reduced by immersion into HI solution (55%, ACS reagent grade, Sigma-Aldrich, USA) in a sealed cuvette that was placed in an oil bath at 95 °C for 1 h. The prepared rGO paper was washed with plenty of DI water and dried in a vacuum oven at 60 °C for 48 h. The rGO paper was then annealed at different temperatures (200, 400, 600, 800, and 1000 °C) in an environment of 15% H_2 in Ar gas in a tube furnace for 30 min. (rGO paper that was not subjected to additional annealing was designated as RT-annealed rGO, or "RT rGO", paper.) The average area and weight of the prepared rGO electrode were 1 cm^2 and 7.7 mg cm^{-2} respectively.

2.2 Characterization

For structural analysis X-ray diffraction (XRD) patterns were collected from 3° to 90° in 2θ with 0.02° steps per s using a Rigaku D/max-3B X-ray diffractometer with Cu-Kα as the radiation source (λ = 0.15406 nm) at 40 kV and 36 mA. Surface morphology was studied using a field emission scanning electron microscope (FESEM JSM-6701F, Jeol Ltd). High-resolution transmission electron microscopy (HRTEM) studies were carried out on a JEOL JEM-2100F microscope. BET surface area measurements were carried out using a Quantachrome, Autosorb-iQ 2ST/MP. X-ray photoelectron spectroscopy (XPS, ESCALAB 250) was performed using focused monochromatized Al Kα radiation (1486.6 eV) and the XPS spectra were fitted using the XPS peak 4.1 software in which a Shirley background was assumed. The elemental bonding of the sample was confirmed by Raman spectroscopy (JY Labram HR 800 spectrometer) using a 632.8 nm wavelength laser. Electrical conductivity measurement was performed using the four-probe method. A Keithley 6512 digital multimeter equipped with a YEW2553DC voltage current standard was used to measure the *I–V* characteristics of the samples at room temperature. The electrochemical measurements for supercapacitors were carried out using an electrochemical cell with a three electrode system. The rGO paper was used as a working electrode with platinum as a counter electrode and Ag/AgCl as a reference electrode in 1 M H_2SO_4 aqueous solution as an electrolyte. Cyclic voltammetry (CV), galvanostatic charge/discharge tests and EIS measurement were performed on ZIVE SP2 LAB analytical equipment (Republic of Korea).

3. Results and discussion

3.1 X-ray diffraction

X-ray diffraction (XRD) was used for structural studies of rGO papers annealed at different temperatures (RT, 200, 400, 600, 800, and 1000 °C). As shown in Fig. 1, the dominant intense peak in the XRD spectra was observed in the 24.48–26.28° range (for annealing temperatures from RT to 1000 °C). This peak corresponded to the graphite phase (002) and indicated high purity, crystallinity, and thermal stability in the rGO paper. Fig. S1 (ESI†) contains the full XRD patterns of RT- and 1000 °C-annealed rGO papers; a few small, nearly negligible peaks were

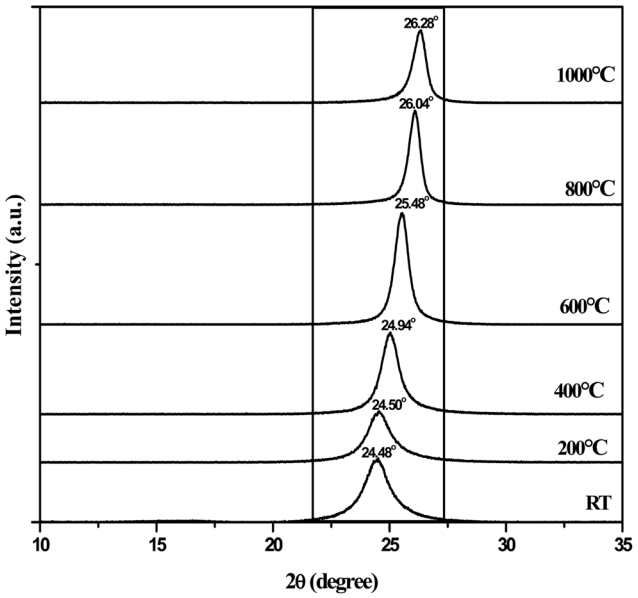

Fig. 1 X-ray diffraction patterns of different temperature annealed rGO papers.

observed at 7.24°, 16.64°, and 50.56° and were attributed to unintentional impurity addition during GO paper reduction using HI. These small peaks diminished during paper annealing, thus suggesting sample purification upon annealing. Peak shifts, which correspond to interlayer distance variation, towards higher degree were observed with increase in annealing temperature. The interlayer distances (d-spacing) were calculated using Bragg's equation ($n\lambda = 2d \sin \theta$) and are presented in Table 1. The d-spacing varied from 3.63 Å to 3.38 Å; these values are close to the reported interlayer distance values for graphene (3.354 Å) and graphite (3.34 Å).[31] Thus, as the annealing temperature was increased, the rGO structure shifted towards the graphene form.[27] Qian *et al.* described the relationship between interlayer distance reduction and electrical conductivity in carbon materials based on total energy and energy band-gap variation.[32] In this study, the electrical conductivity of rGO paper was measured using the four-point probe method; electrical conductivity was found to increase with increasing annealing temperature (Table 1). The enhancement in electrical conductivity was attributed to the reduction in sp^3 clusters and restoration of the graphene-like sp^2 carbon network upon increasing annealing temperature. In other words, sp^3 clusters of rGO sheets disturb electron transport, thereby limiting the mobility and conductivity.[33]

Table 1 Interlayer distance and electrical conductivity of rGO papers annealed at different temperatures

Annealing temperature	Interlayer distance (Å)	Electrical conductivity (S cm^{-2})
RT	3.63	3.6
200 °C	3.61	6.32
400 °C	3.56	10.17
600 °C	3.49	14.41
800 °C	3.41	17.14
1000 °C	3.38	20.93

3.2 Surface morphology

The surface morphology of the rGO paper was studied using field-emission scanning electron microscopy (FESEM). Fig. 2 presents the FESEM cross-section of GO and rGO papers annealed at different temperatures. A photograph of the RT rGO paper is shown in the inset. Both GO and rGO papers exhibited multilayered stacked sheets in the thick layer form. GO papers were well stacked, thick, and compact; however, rGO papers exhibited reduced thickness, or shrinkage, after reduction due to the removal of oxygen-containing functional groups.[25] The thickness of annealed samples increased with increasing annealing temperature. Fig. S2† shows the surface morphology of GO and rGO papers annealed at different temperatures. GO papers exhibited a smooth, wrinkle-free surface morphology, whereas wrinkle formation was evident after reduction, and the extent of wrinkling increased with increasing annealing temperature.

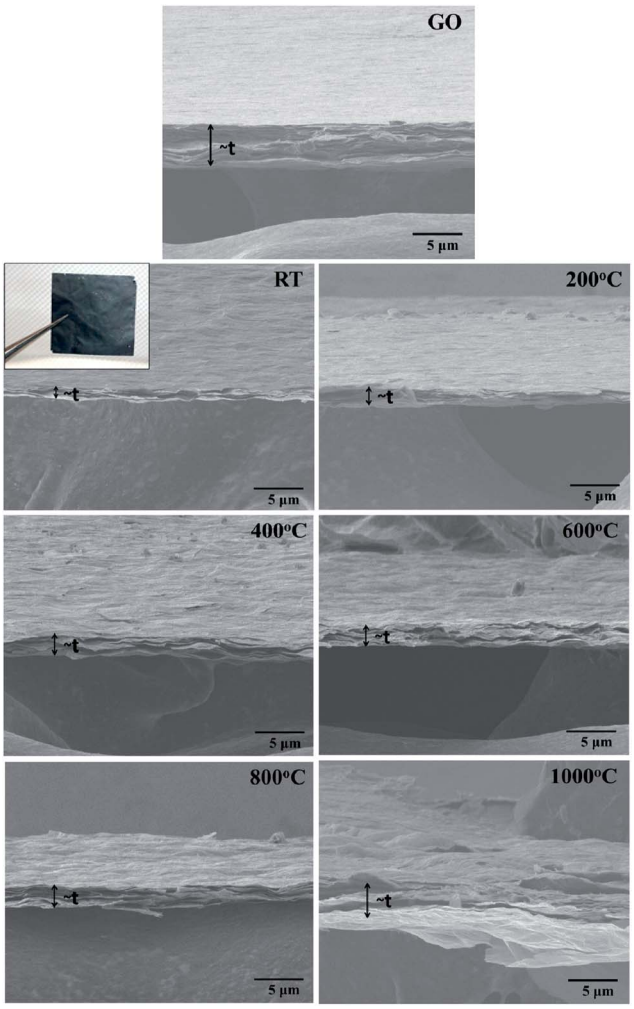

Fig. 2 Cross-section FESEM images of GO and rGO papers annealed at different temperatures. Photograph of RT rGO paper in the inset (20 mm × 20 mm).

High-resolution transmission electron microscopy (HRTEM) was employed for detailed morphological analysis of rGO papers annealed at different temperatures. rGO powder was prepared using the same conditions used for paper preparation. The rGO sheets were dispersed in alcohol, and then the sheets were transferred to a copper HRTEM grid. Fig. 3(a–c) present the HRTEM images of rGO sheets annealed at different temperatures (RT, 200, and 1000 °C). A clear and uniform morphology of RT rGO sheets was observed; indented pinhole spots were detected in 1000 °C-annealed rGO sheets. RT rGO sheets were well dispersed and exhibited few wrinkles in low-magnification HRTEM images; however, under identical sample preparation conditions, 1000 °C-annealed rGO sheets exhibited an increase in wrinkles. The extent of wrinkle formation in the 200 °C-annealed rGO sample was between that of the RT and 1000 °C samples.

In Fig. 2, there seems to be an increase in rGO paper thickness with an increase in annealing temperature. With microfolding as an intrinsic property of reduced graphene sheets, strain formation takes place in a high temperature annealing process and causes the formation of microfoldings along with ripples and wrinkles which gives a crater-like pore surrounding of the thick folded and wrinkled sheets due to the water molecule vaporization, which may cause expansion.[34] But it is clear in TEM images that due to annealing sheets undergo the thermodynamic instability; subsequently, for better stability, they tend to be coupled with each other through a van der Waals interaction with a decrease in interlayer distance.

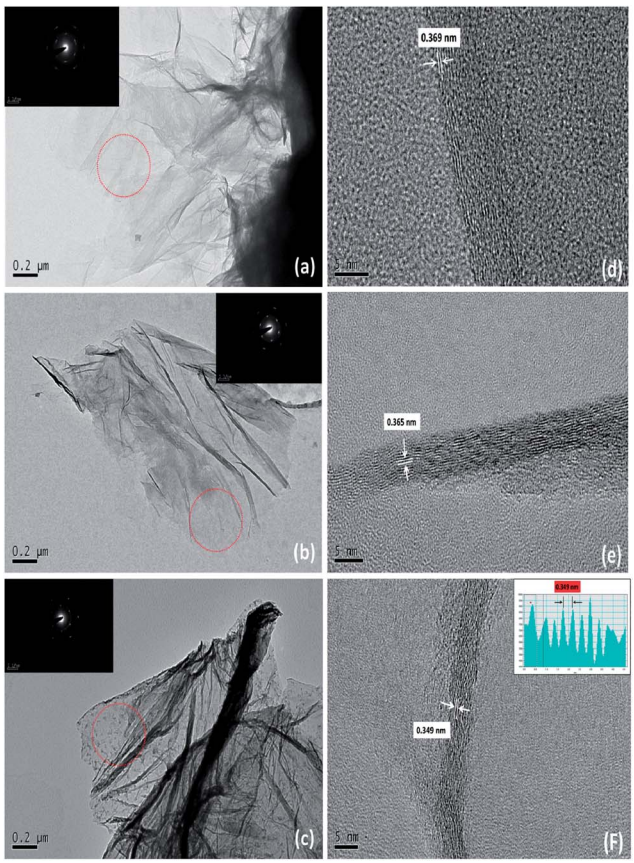

Fig. 3 HRTEM images of rGO sheets annealed at different temperatures: (a) RT, (b) 200 °C, and (c) 1000 °C. SAED patterns in the inset correspond to the region of the rGO sheet marked by the red circle. Cross-sectional view of stacked rGO layers annealed at different temperatures: (d) RT, (e) 200 °C and (f) 1000 °C. The inset shows the number of stacked layers and average interlayer distance.

Selective area electron diffraction (SAED) patterns for RT, 200 °C- and 1000 °C-annealed rGO powder are shown in the insets of Fig. 3(a–c); a crystalline structure was observed in all SAED patterns. A typical sharp ring pattern was observed, along with bright diffraction spots. The first ring originated from the (1100) plane, and the second ring originated from the (1120) plane. The bright spots, which corresponded to the (1100) reflections within the ring, retained the hexagonal symmetry of the [0001] diffraction pattern. The sharp ring pattern and elliptical diffraction spots for the RT rGO sheet exhibited random interlayer orientation and disordered interlayer coherence. The coherence disorder was attributed to decoupling the interactions between the carbon backbones of adjacent layers due to attached functional groups.[35] However, spherical diffraction spots in the patterns of higher temperature (200 and 1000 °C) annealed samples exhibited a hexagonal graphene framework. Fig. 3(d–f) present cross-sectional HRTEM images of stacked rGO layers annealed at different temperatures. The interplanar spacing was 0.369, 0.365, and 0.349 nm for rGO annealed at RT, 200, and 1000 °C, respectively. The interspacing distance decreased with increasing annealing temperature. The inset of Fig. 3(f), which corresponds to the 1000 °C-annealed rGO sample, indicates approximately 11 layers of the stack material in approximately 4.5 nm; the average interlayer distance was 0.349 nm, which is smaller than the distance measured for the RT and 200 °C annealed samples and larger than that of graphite (d_{002} = 0.34 nm). The measured interlayer distances using HRTEM were congruent with the distances measured using XRD.

The BET technique was carried out to measure the surface area of rGO papers annealed at different temperatures. Fig. S3† shows the nitrogen adsorption/desorption isotherm of rGO papers annealed at 200 °C and 1000 °C and the pore size distribution in the inset further demonstrates the porous structure with a high surface area. It is found that, the surface area increases with increase in annealing temperatures. However the variation was very small, *i.e.* 213.7, 264.4, 298.92, 325.4, 376.3 and 432.8 $m^2\ g^{-1}$ for RT, 200, 400, 600, 800 and 1000 °C annealed rGO papers, respectively.

3.3 X-ray photoelectron spectroscopy

X-ray photoelectron spectroscopy (XPS) was used to determine the elemental composition and chemical state of the rGO papers. High-resolution XPS scans were performed for rGO papers annealed at different temperatures, as shown in Fig. S4.† C 1s and O 1s peaks were observed; the intensity of the O 1s peaks deceased with increasing annealing temperature due to the removal of oxygen containing groups during annealing. The C 1s peak was the most prominent carbon-containing peak in all samples. The C–C and C–H binding energy was in the range

of 284.5–285 eV, and the observed chemical shifts at +1.5, +2.5, and +4.0 eV were characteristic of C–OH, C═O, and O═C–OH functional groups, respectively.[36] For more detailed analysis, C 1s peaks were deconvoluted using a fitting software program, and the obtained spectra are shown in Fig. 4. Deconvolution of the C 1s XPS spectra of rGO papers annealed at different temperatures revealed the presence of five main components that corresponded to carbon atoms with different functional groups. Specifically, the peak at 284.45 eV was attributed to the binding energy of the non-oxygenated ring C–C, C═C, and C–H bonds, and the deconvoluted peaks centered at 285.5, 286.4, 287.9, and 288.9 eV were assigned to the C–O–C, C–O, C═O, and O–C═O functional groups, respectively. The peak area ratios of the C–O, C═O, and O–C═O bonds to the C–C bond were calculated to determine the concentration of functional groups at different annealing temperatures; the results are summarized in Table 2. Based on the C 1s peaks, RT rGO paper contained considerable oxygen-containing functional groups.

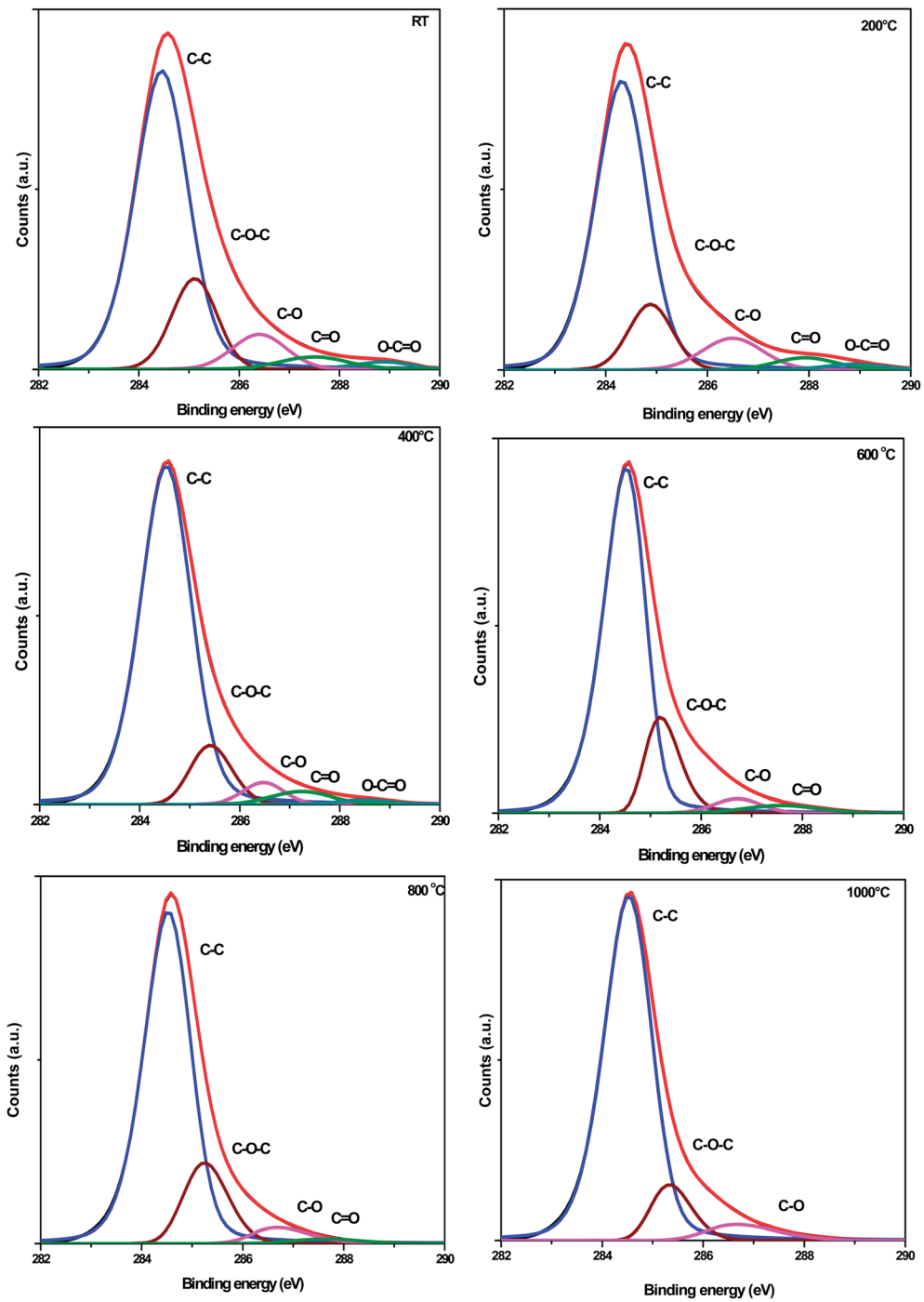

Fig. 4 Deconvoluted C 1S XPS spectra of different temperature annealed rGO papers.

Table 2 The peak area (*A*) ratios of the oxygen-containing bonds to the C–C bonds of rGO papers annealed at different temperatures

Annealing temperature	A_{C-O-C}/A_{C-C}	A_{C-O}/A_{C-C}	$A_{C=O}/A_{C-C}$	$A_{O-C=O}/A_{C-C}$
RT	0.255771	0.117119	0.051205	0.024064
200 °C	0.191725	0.126006	0.047615	0.02031
400 °C	0.142609	0.05163	0.043568	0.012628
600 °C	0.228312	0.038169	0.045483	—
800 °C	0.22948	0.056904	—	—
1000 °C	0.13689	0.065592	—	—

The presence of C–OH, C–O, and C=O oxygen-containing functional groups decreased with increasing annealing temperature and completely disappeared at 1000 °C, indicating considerable deoxygenation during high-temperature annealing. However, the presence of C–O–C and C–O peaks in rGO paper annealed at 1000 °C reflected incomplete deoxygenation; residual oxygen groups persisted in basal plane carbon atoms and were very difficult to remove.[35,37]

3.4 Raman analysis

Raman analysis was performed to determine the influence of annealing temperature on the sp^2 domains of rGO paper; the results of the Raman analysis are presented in Fig. 5. Prominent spectral features, specifically G and D bands, were observed. In addition, two minor peaks at 2719 cm^{-1} (2D) and 2926 cm^{-1} (S3) were observed and are shown in the inset. The relatively sharp G and D features of the sp^2 sites dominated the Raman spectra of all disordered carbons. The peak near 1350 cm^{-1} is associated with the D band and was attributed to the in-plane carbon-ring breathing (A_{1g}) mode, which is forbidden in perfect graphite. The G and 2D peaks correspond to the E_{2g} vibrational and out-of-plane modes within aromatic carbon rings, respectively. The G band was attributed to the degenerate optical phonon mode at the Brillouin zone center, which was induced by a single resonance process that requires scattering at defect sites to conserve momentum.[38,39] The dominant peaks in the D mode spectra originated from phonons between the K and M points of the Brillouin zone. The D mode is dispersive; it varies with photon excitation energy, even when the G peak is not dispersive, and its intensity is strictly connected to the presence of six-fold aromatic rings. The G band corresponds to graphite-like sp^2 carbon atoms, and the D band corresponds to disordered sp^2 carbons for which the disorder was induced by linking with sp^3 carbon atoms. The D peak provided information about the relative amount of surrounding sp^3 carbons, *i.e.*, defects, such as impurity atoms, functional groups, heptagon–hexagon pairs, folding, *etc.*, in the rGO. The association between the D and G peaks generated a G_0 peak near 2926 cm^{-1}.[39] Upon annealing, the G band intensity did not significantly change, but the intensity of the D band increased. The prominent D peak in the Raman spectra was also attributed to structural imperfections. The G bands were red-shifted from 1605 cm^{-1} to 1590 cm^{-1} as the annealing temperature increased from RT to 1000 °C. The observed red shifting in the G band at higher annealing temperatures was attributed to thermal expansion-induced volume changes.[40,41] These Raman results are consistent with the FESEM results. The red shifting could also be attributed to clustering of the sp^2 phase, *i.e.*, to the formation of a more ordered structure upon annealing,[41] thus indicating a connection between the Raman and XPS results. Table S1† contains the I_D/I_G ratios of rGO papers annealed at different temperatures. The I_D/I_G ratio was 1.07 for RT rGO paper and 1.2 for 1000 °C-annealed rGO paper, thus indicating that the annealing process altered the structure of rGO paper from one with a high quantity of sp^3 structural defects to one with a greater presence of sp^2 clusters.[24,42]

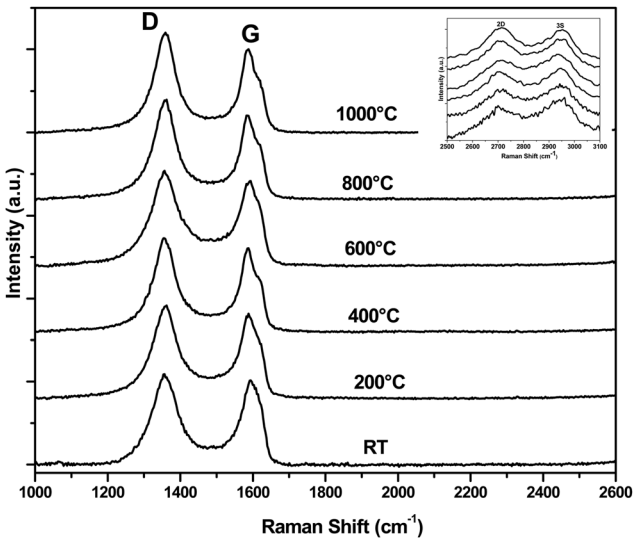

Fig. 5 Raman spectra of different temperature annealed rGO papers.

Hydrogen gas has GO reduction ability especially at high temperature,[43] Fig. S5† shows the Raman spectra of rGO papers annealed at 200 °C and 1000 °C in the mixture of argon and hydrogen and only an argon gas environment. Raman study reveals that there is no change in Raman spectra for rGO paper annealed at 200 °C however, samples annealed at high temperature (1000 °C) show increase in Raman intensity. It signifies that hydrogen helps to reduce again to rGO paper more at high temperature compared to samples annealed without hydrogen, but this effect is negligible at 200 °C for annealed rGO paper.

3.5 Supercapacitance performance of rGO paper

Supercapacitor performance of different temperature annealed rGO paper measurements were carried out using a three-electrode electrochemical cell, in which rGO papers were used as the working electrode attached on a stainless steel current collector substrate by using polytetrafluoroethylene as a binder. Platinum was the counter electrode, and Ag/AgCl/NaCl was the reference electrode in a 1 M H_2SO_4 electrolyte. The influence of scan rate on the specific/interfacial capacitance was evaluated for each sample. The specific capacitance (F g^{-1}) of each electrode was obtained by dividing its capacitance by the weight of

the electrode. The interfacial capacitance (F cm^{-2}) was obtained by dividing the capacitance by the area of the electrode dipped in the electrolyte.

Fig. 6(a–f) show the typical cyclic voltammetric (CV) behavior of rGO paper samples annealed at different temperatures in 1 M H_2SO_4 at 50 mV s^{-1} within an optimized potential range of −400 to +600 mV *versus* Ag/AgCl. An ideal capacitor displays a rectangular CV curve arising from EDLC, and nearly rectangular CV curves with small redox peaks (from −3.5 to +3 mV) indicate pseudocapacitive behavior.[44] As shown in the CV curves of Fig. 6(a and b), rGO papers annealed at RT and 200 °C exhibited both pseudocapacitance and EDLC. The rGO paper annealed at 200 °C exhibited the maximum current under the curve with a symmetric CV.[34] However, as shown in Fig. 6(c–f), the redox peak fades in the CV curves of the rGO papers annealed at temperatures of 400 °C and higher, thereby indicating that the

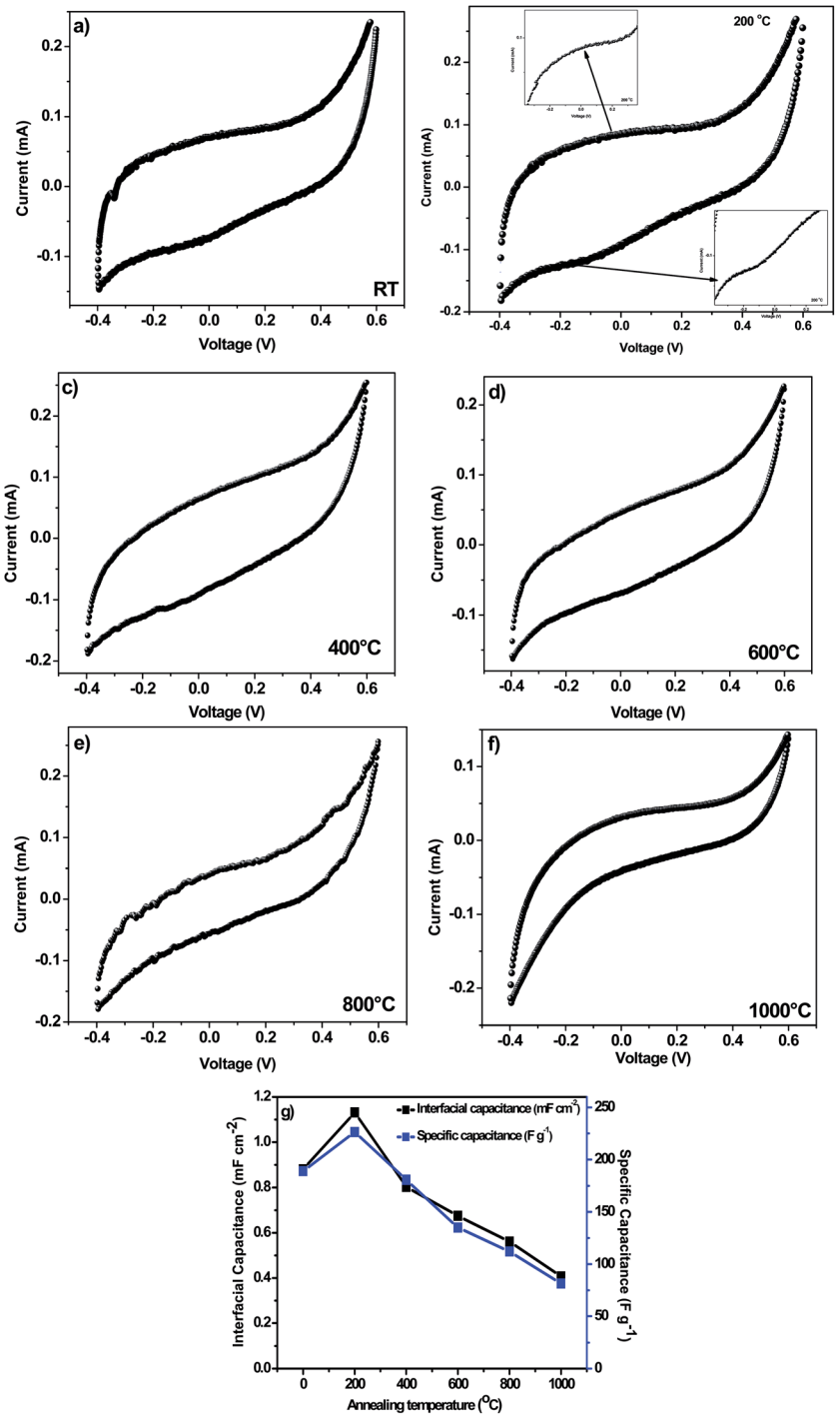

Fig. 6 Cyclic voltammetric behavior of rGO papers annealed at different temperatures (a–f). The graph of interfacial and specific capacitance for all samples calculated from CV curves (g).

EDLC dominates over the pseudo-capacitance. The enlarged image of cyclic voltammetry (CV) for redox peaks of rGO papers annealed at 200 °C shown in Fig. S6.† As the annealing temperature increased, the relative dominance of EDLC compared to pseudocapacitance increased. As shown in Fig. 6(g), interfacial and specific capacitances for all samples were calculated from the CV curves. Increases in interfacial and specific capacitances were observed in the sample annealed at 200 °C; however, interfacial and specific capacitances of rGO papers decreased upon annealing at higher temperatures (400 °C and above). The maximum specific and interfacial capacitances were observed for rGO papers annealed at 200 °C and were 225 F g^{-1} and 1.19 mF cm^{-2}, respectively.

The charge–discharge performance of rGO papers annealed at different temperatures was evaluated within a potential window of 0.0 to +1.0 V *versus* Ag/AgCl at a current density of 100 μA cm^{-2}. Fig. 7 shows the characteristic potential curves *versus* cycle time for the rGO paper electrodes. The appearance of non-linear charge–discharge plots with small variation in voltage (IR) drops shows pseudocapacitive behavior of the rGO paper electrodes. The graph in the inset of Fig. 7 plots the interfacial and specific capacitances calculated from different temperature annealed rGO papers' charge–discharge curves. The maximum specific and interfacial capacitances for rGO annealed at 200 °C were 1.4 mF cm^{-2} and 198 F g^{-1}, respectively. These values for specific and interfacial capacitances were close to those calculated by CV analysis. Typical Ragone plots of the different temperature annealed samples are included in Fig. S7.† The charge–discharge performance at different charging current densities (100, 250, and 500 μA cm^{-2}) for rGO papers annealed at 200 °C was evaluated, and the results are shown in Fig. 8. The IR drop of the charge–discharge curve increased with increasing charging current density. The Ragone plot of energy and power densities calculated from the charge–discharge curves for different charging current densities

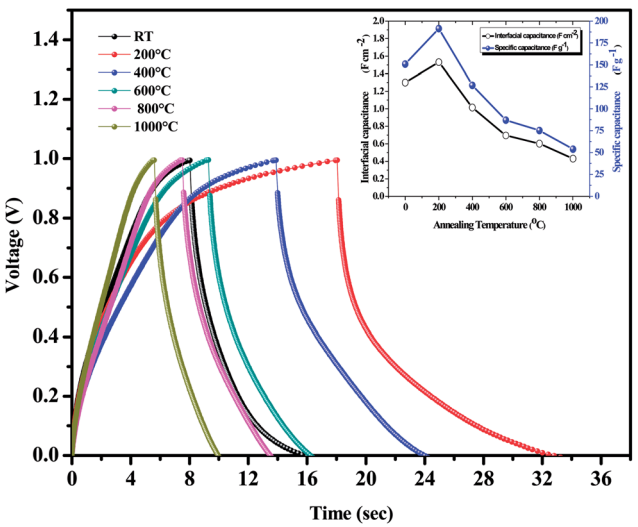

Fig. 7 Charge–discharge performance of rGO papers annealed at different temperatures. The graph of interfacial and specific capacitances calculated from charge–discharge curves in the inset.

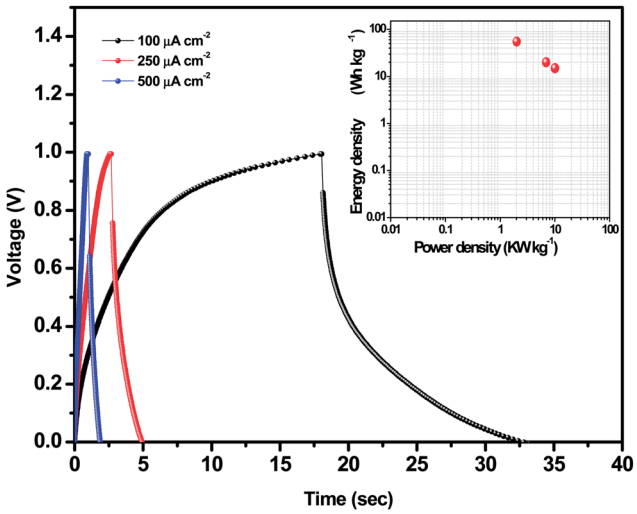

Fig. 8 Charge–discharge performance at different charging current densities for rGO annealed at 200 °C. The Ragone plot of energy and power densities calculated from the charge–discharge curve for different charging current densities in the inset.

is shown in the inset of Fig. 8. The optimum energy and power densities were 20 Wh kg^{-1} and 32 kW kg^{-1}, respectively; these values are superior to those previously reported for pure graphene and GO.[13,45]

3.6 Impedance analysis

To further elucidate the electrochemical performance of rGO papers, the ion diffusion kinetics was investigated using electrochemical impedance spectroscopy. Fig. 9 shows the Nyquist plots of rGO papers annealed at temperatures from RT to 1000 °C in 1 M H_2SO_4 in the frequency range of 1–0.01 Hz; expanded views of the high-frequency region are shown in the insets of Fig. 9. Nearly vertical impedance lines in the low-frequency region indicated good capacitor behavior in the cell. The negligible high-frequency resistor–capacitor (RC) loops (or semicircles) indicated good electrode contact. The very small solution resistance (R_s) value (approximately 1.4 Ω) obtained from the *x*-intercept of the Nyquist plots suggested that the rGO paper electrodes exhibited very low resistance and good ion response. The R_s values decreased from 1.14 to 0.78 Ω with increasing annealing temperature from RT to 1000 °C, thus indicating an increase in rGO conductivity with increasing annealing temperature. An RC loop was observed for the RT rGO sample but mostly disappeared in samples annealed at 200 °C and above. A small RC loop was observed for the 1000 °C-annealed rGO sample, which was attributed to the creation of large pores upon removal of hydroxyl and carboxyl groups from the interior of the rGO paper.

The removal of epoxide, hydroxyl, and carboxyl groups from rGO papers upon annealing, and the consequent influence on sample conductivity and specific capacitance is shown in Fig. 10. The conductivity of rGO papers was inversely proportional to the O 1s/C 1s atomic ratio, which was attributed to the transformation of rGO towards pure graphene with increasing

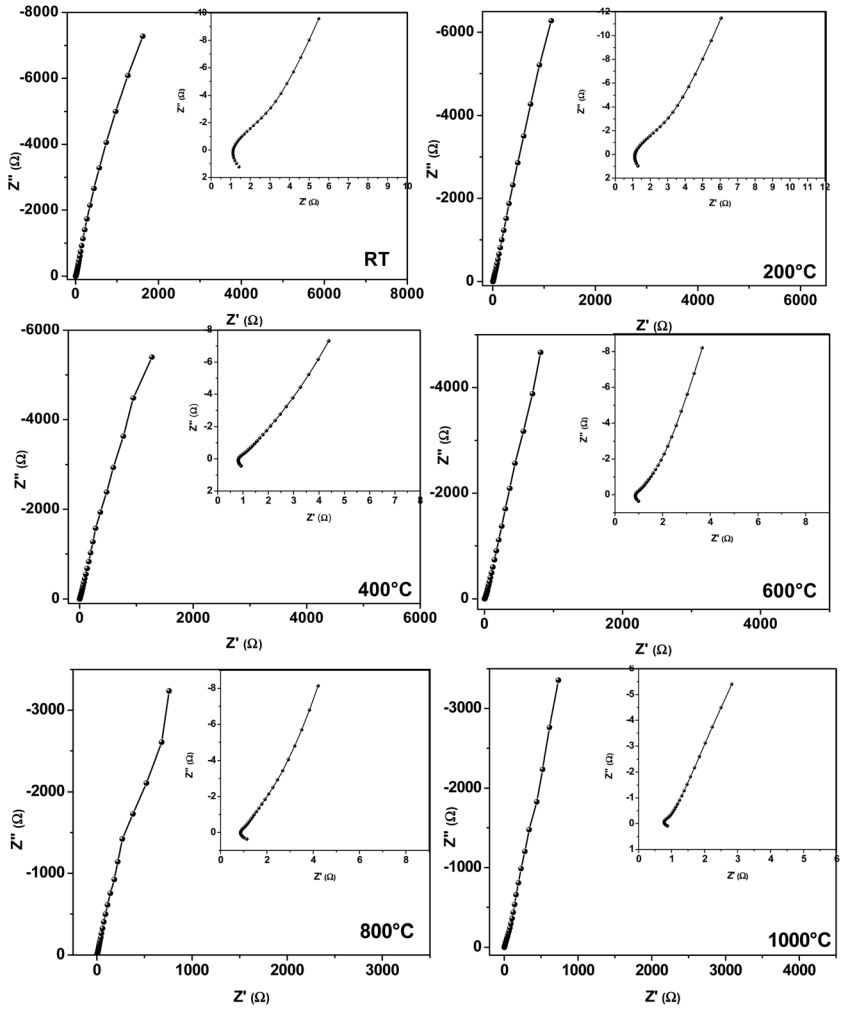

Fig. 9 Nyquist plots of different temperature annealed rGO papers with an expanded view of the high-frequency region in the inset.

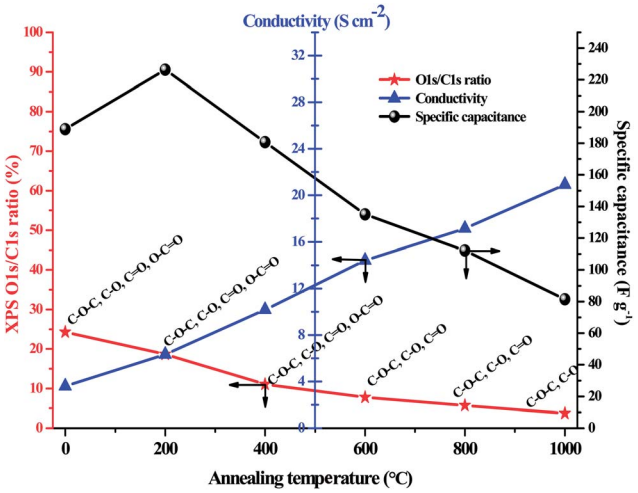

Fig. 10 Annealing temperature effects on the XPS O 1s/C 1s ratio, electrical conductivity and specific capacitance of rGO papers.

annealing temperature.[23,46] The specific capacitance of the rGO paper depended on both the conductivity and the presence of attached functional groups. The capacitance decreased in rGO papers annealed at temperatures higher than 200 °C due to a concurrent decrease in the presence of attached functional groups (*i.e.*, a deduction in the O 1s/C 1s ratio), which are responsible principally for pseudocapacitance. On the other hand, RT rGO papers also exhibited low capacitance due to their low conductivities. These results suggested that the optimization of both conductivity and the presence of attached functional groups are essential for achieving maximum specific capacitance in rGO papers. In this study, the rGO paper annealed at 200 °C was identified as a potential superior electrode material for supercapacitors due to its ideal combination of EDLC and pseudocapacitance.

4. Conclusions

In this study, we evaluated the influence of annealing temperature on rGO paper properties in terms of the removal of attached functional groups and electrical conductivity enhancement, both of which affect the specific capacitance of the material. The dominant graphite phase peak (002) in the XRD patterns shifted towards a higher degree as the annealing temperature increased from RT to 1000 °C, thus indicating

interlayer distance reduction. Interlayer distance values determined by XRD and HRTEM were congruent to each other. FESEM and BET analyses indicated the morphological and surface area of rGO paper adaptation with temperature, respectively. Dramatic changes in the chemical state of the material were observed by XPS, *i.e.* the attached hydroxyl, carboxyl, and other oxygen-containing groups in rGO paper decreased with increasing annealing temperature. The rGO paper supercapacitor performance was found to be interlinked with its conductivity and attached functional groups. Their ideal combination was observed in rGO paper annealed at 200 °C, which exhibited both EDLC and pseudocapacitance and a specific capacitance of approximately 198 F g^{-1} in a 1 M H_2SO_4 electrolyte at a 50 mV s^{-1} scan rate. Thus, annealing of rGO paper will be useful for the fabrication of highly efficient and environmentally friendly electrodes for energy-storage applications.

Acknowledgements

This work was supported by the National Research Foundation of Korea (NRF) grant funded by the Korean government (MEST) (NRF-2011-0017673).

References

1 M. Z. Jacobson, *Energy Environ. Sci.*, 2009, **2**, 148–173.
2 E. Frackowiak and F. Beguin, *Carbon*, 2002, **40**, 1775–1787.
3 N. Jha, P. Ramesh, E. Bekyarova, M. E. Itkis and R. C. Haddon, *Adv. Energy Mater.*, 2012, **2**, 438–444.
4 Z. Lei, Z. Liu, H. Wang, X. Sun, L. Lu and X. S. Zhao, *J. Mater. Chem. A*, 2013, **1**, 2313–2321.
5 C. H. Kim, S. I. Pyun and H. C. Shin, *J. Electrochem. Soc.*, 2002, **149**, A93–A98.
6 H. Probstle, C. Schmitt and J. Fricke, *J. Power Sources*, 2002, **105**, 189–194.
7 Q. A. Li, R. R. Jiang, Y. Q. Dou, Z. X. Wu, T. Huang, D. Feng, J. Yang, A. Yu and D. Zhao, *Carbon*, 2011, **49**, 1248–1257.
8 L. Xu, N. Wei, X. Xu, Z. Fan and Y. Zheng, *J. Mater. Chem. A*, 2013, **1**, 2002–2010.
9 C. Nanjundiah, P. Bendale, M. R. Malay, J. M. Dispennette and E. Chaney, *US Pat.* US6643119 B2, 2003.
10 E. R. Buiel, V. Eshkenazi, L. Rabinovich, W. Sun, V. Vichnyakov, A. J. Swiecki and J. E. Cole, *US Pat.* US7881042 B2, 2011.
11 Y. Korenblit, M. Rose, E. Kockrick, L. Borchardt, A. Kvit, S. Kaskel and G. Yushin, *ACS Nano*, 2010, **4**, 1337–1344.
12 M. Endo, T. Takeda, Y. J. Kim, K. Koshiba and K. Ishii, *Carbon Science*, 2001, **1**, 117–128.
13 C. Liu, Z. Yu, D. Neff, A. Zhamu and B. Z. Jang, *Nano Lett.*, 2010, **10**, 4863–4868.
14 M. F. El-Kady, V. Strong, S. Dubin and R. B. Kaner, *Science*, 2012, **335**, 1326–1330.
15 X. Yang, C. Cheng, Y. Wang, L. Qiu and D. Li, *Science*, 2013, **341**, 534–537.
16 X. Lin, X. Shen, Q. Zheng, N. Yousefi, L. Ye, Y.-W. Mai and J.-K. Kim, *ACS Nano*, 2012, **6**, 10708–10719.
17 G. Ning, C. Xu, Y. Cao, X. Zhu, Z. Jiang, Z. Fan, W. Qian, F. Wei and J. Gao, *J. Mater. Chem. A*, 2013, **1**, 408–414.
18 O. C. Compton, D. A. Dikin, K. W. Putz, L. C. Brinson and S. T. Nguyen, *Adv. Mater.*, 2010, **22**, 892–896.
19 H. Chen, Z. Song, X. Zhao, X. Li and H. Lin, *RSC Adv.*, 2013, **3**, 2971–2978.
20 D. Li, M. B. Müller, S. Gilje, R. B. Kaner and G. G. Wallace, *Nat. Nanotechnol.*, 2008, **3**, 101–105.
21 H. Chen, M. B. Müller, K. J. Gilmore, G. G. Wallace and D. Li, *Adv. Mater.*, 2008, **20**, 3557–3561.
22 I.-K. Moon, J. Lee, R. S. Ruoff and H. Lee, *Nat. Commun.*, 2010, **1**, 1–6.
23 H. Feng, R. Cheng, X. Zhao, X. Duan and J. Li, *Nat. Commun.*, 2013, **4**, 1–7.
24 D. Sun, X. Yana, J. Lang and Q. Xue, *J. Power Sources*, 2013, **222**, 52–58.
25 C. Valles, J. D. Nunez, A. M. Benito and W. K. Maser, *Carbon*, 2012, **50**, 835–844.
26 H.-P. Cong, X.-C. Ren, P. Wang and S.-H. Yu, *Energy Environ. Sci.*, 2013, **6**, 1185–1191.
27 T. Hu, X. Sun, H. Sun, M. Yu, F. Lu, C. Liu and J. Lian, *Carbon*, 2013, **51**, 322–326.
28 N. A. Kumar, H. J. Choi, Y. R. Shin, D. W. Chang, L. Dai and J. B. Baek, *ACS Nano*, 2012, **6**, 1715–1723.
29 C. Xiang, M. Li, M. Zhi, A. Manivannan and N. Wu, *J. Power Sources*, 2013, **226**, 65–70.
30 W. Zhou, J. Liu, T. Chen, K. S. Tan, X. Jia, Z. Luo, C. Cong, H. Yang, C. M. Li and T. Yu, *Phys. Chem. Chem. Phys.*, 2011, **13**, 14462–14465.
31 Y. Shibuta and J. A. Elliott, *Chem. Phys. Lett.*, 2011, **512**, 146–150.
32 Y. Qian, K. T. Lam, C. Lee and G. Liang, *Carbon*, 2012, **50**, 165–166.
33 C. Mattevi, G. Eda, S. Agnoli, S. Miller, K. A. Mkhoyan, O. Celik, D. Mastrogiovanni, G. Granozzi, E. Garfunkel and M. Chhowalla, *Adv. Funct. Mater.*, 2009, **19**, 2577–2583.
34 F. Liu, S. Song, D. Xue and H. Zhang, *Adv. Mater.*, 2012, **24**, 1089–1094.
35 A. Ganguly, S. Sharma, P. Papakonstantinou and J. Hamilton, *J. Phys. Chem. C*, 2011, **115**, 17009–170019.
36 S. Yumitori, *J. Mater. Sci.*, 2000, **35**, 139–146.
37 D. Yang, A. Velamakanni, G. Bozoklu, S. Park, M. Stoller, R. D. Piner, S. Stankovich, I. Jung, D. A. Field, C. A. Ventrice Jr and R. S. Ruoff, *Carbon*, 2009, **47**, 145–152.
38 T.-C. Chiang and F. Seitz, *Ann. Phys.*, 2001, **10**, 61–74.
39 A. Jorio, M. Dresselhaus, R. Saito and G. F. Dresselhaus, *Raman spectroscopy in graphene related system*, Wiley-VCH, 2011.
40 I. Calizo, S. Ghosh, W. Z. Bao, F. Miao, C. N. Lau and A. A. Balandin, *Solid State Commun.*, 2009, **149**, 1132–1135.
41 T. V. Cuong, V. H. Pham, Q. T. Tran, J. S. Chung, E. W. Shin, J. S. Kim and E. J. Kim, *Mater. Lett.*, 2010, **64**, 765–767.
42 A. Wei, J. Wang, Q. Long, X. Liu, X. Li, X. Dong and W. Huang, *Mater. Res. Bull.*, 2011, **46**, 2131–2134.
43 S. Pei and H.-M. Cheng, *Carbon*, 2012, **50**, 3210–3228.
44 H.-J. Choi, S.-M. Jung, J.-M. Seo, D. W. Chang, L. Dai and J.-B. Baek, *Nano Energy*, 2012, **1**, 534–551.
45 B. Xu, S. Yue, Z. Sui, X. Zhang, S. Hou, G. Cao and Y. Yang, *Energy Environ. Sci.*, 2011, **4**, 2826–2830.
46 A. Bagri, C. Mattevi, M. Acik, Y. J. Chabal, M. Chhowalla and V. B. Shenoy, *Nat. Chem.*, 2010, **2**, 581–587.

